Modeling of plasticity and ductile fracture physical mechanisms and numerical simulation of laboratory specimens

Gilles Rousselier

To cite this version:

Gilles Rousselier. Modeling of plasticity and ductile fracture physical mechanisms and numerical simulation of laboratory specimens. 24ème Congrès Français de Mécanique, Aug 2019, Brest, France. ⟨hal-02401455⟩

HAL Id: hal-02401455
https://minesparis-psl.hal.science/hal-02401455v1

Submitted on 10 Dec 2019

Modeling of plasticity and ductile fracture physical mechanisms and numerical simulation of laboratory specimens (1)

G. ROUSSELIER

MINES ParisTech, PSL University, MAT-Centre des Matériaux, CNRS UMR 7633,
BP87, 91003 Evry Cedex, France, gilles.rousselier@mines-paristech.fr

Abstract

The most commonly observed ductile fracture mechanism is void nucleation, growth and coalescence. Fully coupled "porous plasticity" models (GTN, Rousselier) are presented and their limits are discussed in relation with quantitative observations and micromechanical simulations. Strain localization in a macroscopic planar band represents the void coalescence phase. (Micromechanical modeling of nucleation is not presented.) These models are well suited for laboratory specimen calculations, including the multi-scale version with a reasonable computation time due to reduced texture identification (8 to 15 crystal orientations). A trans-granular crystallographic ductile fracture mechanism is also modeled in the multi-scale framework.

Examples of numerical simulations are given for aluminum and steel specimens. The experimental and numerical results are in good agreement with regard to fracture strains and locations as well as macroscopic/microscopic features. The effect of the carbides-nucleated secondary population of voids in low alloyed steels is modeled in the multi-scale framework and used in calculations.

Keywords: porous plasticity; strain localization; Coulomb-Rousselier ductile fracture model; submicron voids; finite elements;

---

(1) English version of: G. Rousselier. Modélisation des mécanismes physiques de plasticité et de rupture ductile et simulation numérique des essais de laboratoire. 24th Congrès Français de Mécanique, Aug. 2019, Brest, France. 12 p., 2019.

1 Introduction

Plasticity and ductile fracture are closely related. Indeed, ductile failure can be defined in a very general way as a damage mechanism involving a gradual and significant dissipation of mechanical energy, at several scales. The most commonly observed (but not unique) ductile failure mechanism is nucleation, growth (by plastic deformation) and coalescence of microscopic voids. The most widely used macroscopic criterion of plasticity is the one of von Mises, extended to the case of a spherical void by Gurson [1]. These two models have been generalized to the cases of work hardening (flow stress depending on plastic deformation) and anisotropic material (Hill's plasticity criterion, non-spherical voids).

However, these generalized models do not take into account the hardening anisotropy at large strain (distortion of the yield surface, non-proportional loading path), a problem that arises even for an initially isotropic material. Besides, the Gurson model is theoretically valid only for the very beginning of the plastic deformation. At least one adjustable parameter q_1 must be added to increase cavity growth [2]. Moreover, the analytical form of the Gurson model is not well suited for strain localization in a plane of deformation, at large stress triaxiality; the volume strain rate must be further increased by an ad hoc equation in the modified GTN model [3]. At small stress triaxiality, this model gives a damage that is much too small (and it completely disappears at zero stress triaxiality), despite the modifications.

Macroscopic models of plasticity seem to be close to their limits. On the contrary, in polycrystalline plasticity, the evolution of anisotropy and the distortion of the load surface as well as the non-proportional loadings are modeled. The main difficulty is the computation time, both for parameter identification and for finite element calculations. The mechanical behavior can now be modeled with a very small number of crystalline orientations, from 8 to 15 depending on the material [4,5]. The hardening parameters and the ones of the reduced texture (Euler angles and volume fractions) are simultaneously identified by inverse optimization from mechanical tests only (the experimental texture is not used). Numerical simulation in polycrystalline plasticity of laboratory tests is then possible in a reasonable time.

Due to its quadratic dependence on von Mises equivalent stress, integration of the Gurson model into the polycrystalline framework is not possible. Without additional parameter or equation, the Rousselier model [6,7,22] gives strain localization in a plane at all stress triaxialities, a significant void damage at small stress triaxiality, and it can be integrated into the polycrystalline framework [8,9]. This framework also enables multi-scale modeling of other mechanisms of plasticity, for example dynamic strain aging [10], or ductile failure, for example the trans-granular crystallographic fracture observed in particular in aluminum thin sheets [8,11] or the effect of a second population of submicron voids in steels and aluminum alloys.

Ductile fracture macroscopic models (Rice-Tracey, Gurson, GTN, Rousselier) are presented and discussed in Section 2. Multi-scale modeling of several ductile failure mechanisms is presented in Section 3. Section 4 brings together two examples of application to aluminum alloys and low alloyed steels.

2 Ductile fracture macroscopic modeling

The founding model is that of Rice and Tracey [12] which gives the growth rate of an isolated spherical void of radius R (transposable to the volume fraction f) as a function of the stress triaxiality η:

$$\dot{f} / f = 3\dot{R}/R = \dot{p} D_1 \exp(Q\eta), \qquad \eta = \sigma_m / \sigma_p , \qquad \dot{p} = \dot{\varepsilon}_{eq}^{p} \quad \text{(von Mises)} \tag{1}$$

σ_p is the plastic flow stress, a constant in the original model. The constant parameters are $Q = 1.5$ and $D_1 = 1.28$ (Huang's corrected value [13]). This model is in agreement with void growth measurements of the 1980s, confirmed since 20 years by X-ray tomography, with however a larger $D_1 = 1.5$ to 2. It is therefore a solid reference.

The Gurson model [1,2] is a plastic flow surface obtained by homogenization of a hollow sphere with two kinematic fields (displacement rates):

$$\sigma_{eq}^2 / \sigma_p^2 - (1 + q_3 f^2) + 2 q_1 f \cosh(Q q_2 \eta) = 0 , \; 3\dot{\varepsilon}_m^p = \dot{f} /(1-f) = 2 \dot{p} D_1 f \sinh(Q q_2 \eta) \tag{2}$$

In the original model, q_1=q_2=q_3=1. The flow stress $\sigma_p(p)$ takes into account work hardening in the GTN model [3]. The second equation (2_2) is given by the mass conservation law and the normality hypothesis. The parameters are Q = 3/2 and D_1 = $3q_1q_2/4$. With the values recommended by Tvergaard [2]: q_1=1.5, q_2=1, q_3=q_1^2, we obtain D_1 = 1.125, which remains too small compared to the measurements (all the more with 2sinh < exp). These values were selected to improve the agreement with numerical studies of materials containing periodically distributed circular cylindrical voids *in a shear band* [2], which is somewhat paradoxical for a model mainly used at large stress triaxiality to achieve strain localization in a plane normal to the main loading direction. Nevertheless, they are used in almost all publications.

In a finite element mesh, void coalescence is modeled by macroscopic strain localization in a plane [6,3]. Finite element calculations of cells with a spherical void by Koplik and Needleman [14] show that coalescence corresponds to the transition to *uniaxial deformation* for $f = fc$ values that *depend on stress triaxiality* (their calculations are for η = 1, 2 and 3). For a plane normal to the main loading direction, without shear, this results in a necessary condition [8,9], the left equation (3_1):

$$\dot{\varepsilon}_m^p \cong \dot{\varepsilon}_{eq}^p / 2, \qquad \dot{\varepsilon}_m^p \le \dot{\varepsilon}_{eq}^p / 2 \;\; (\dot{\varepsilon}_m^p = 0 \text{ is possible}) \tag{3}$$

When the plane is inclined and the shear rates are not zero, equality (3_1) is replaced by inequality (3_2); ductile fracture becomes possible without voids and with $\dot{\varepsilon}_m^p = 0$, but voids are not excluded. The Thomason-like coalescence models [15] satisfy the equality (3_1). These coalescence models can be coupled with the GTN model, but their analytical expressions include a major difficulty: the localization plane must be known in advance; failing this, as many models of coalescence as possible localization plans are required, which considerably limits the use of these coupled models.

The consequences of this necessary kinematic condition of macroscopic localization (NKCML) are important. The yield surface of the Gurson model is plotted in Fig. 1 for a fairly large value $f = 0.1$. On the black curve, at large stress triaxiality, coalescence in a plane is impossible because $\dot{\varepsilon}_m^p$ cannot be larger than $\dot{\varepsilon}_{eq}^p/2$. Large values of f are required for the Gurson model to achieve localization *in a plane* at large stress triaxiality (the NKCML is *not* achieved either for large values of f, but the finite element discretization could transform the GTN model *punctual* localization into a *planar volumic* localization). So, the *discontinuous* increase of the rates $\dot{f}$ and $\dot{\varepsilon}_m^p$ of the GTN model for $f = f$c, multiplied by an adjustable factor K (also noted δ in the literature), violates the law of normality but makes it possible to achieve localization in a plane. Note that only the non-accelerated value f and not the accelerated one f* is to be compared with experimental data. This model of critical void volume fraction $f = f$c does not agree with the results of Koplik and Needleman [14].

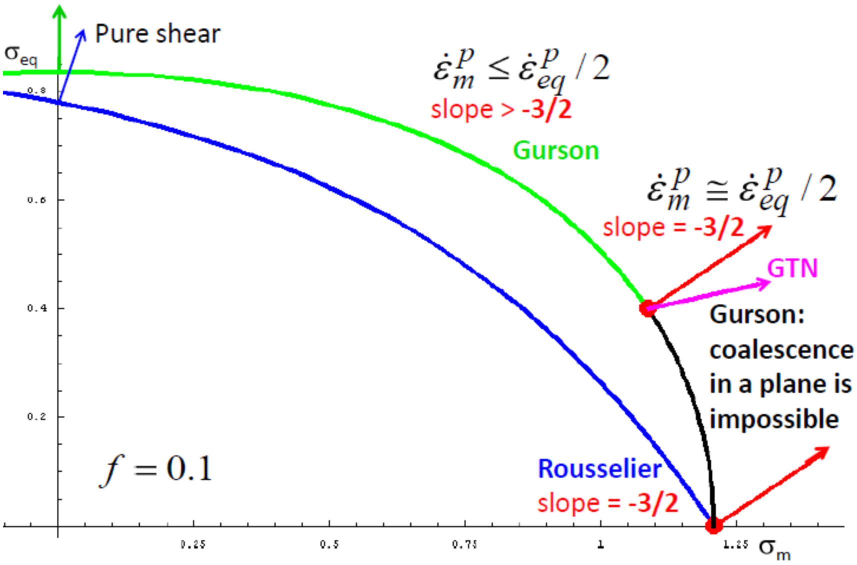

Figure 1. Yield surfaces in porous plasticity with f=0.1, σ_p=1. Modified Gurson model with q_1=1.6245, q_2=1, q_3=2.25 (green and black curves). Rousselier model with σ_1=(2/3)σ_p and D_1=2 (blue curve). Red arrows (plastic flow direction) correspond to the NKCML, Eq. (3_1). Effect on plastic flow direction of the GTN model void growth acceleration function with K=δ=3, loss of normality.

In the same way as for $f > f$c, the addition of a void nucleation model *at very large strain* p>pc:

$$\dot{f} = \dot{f}.growth + \dot{f}.nucleation = 3(1-f)\dot{\varepsilon}_m^p + A(p)\dot{p} \tag{4}$$

increases f and thus also makes it possible to achieve localization. It also facilitates the strain localization in shear, which is not obtained with the GTN model alone. But this nucleation model should not be manipulated for these purposes, it should remain restricted to modeling the effect of a second population of voids with late nucleation.

All these additional features, sometimes questionable, eventually make the Gurson model operational, at the cost of increased complexity and a certain arbitrariness in the choice of many adjustable parameters. At small stress triaxiality and despite the q_1 and q_2 parameters, this model gives much too little damage; the damage is zero at zero stress triaxiality, because of the hyperbolic sine function, Eq. (2_2).

Like Gurson's, the Rousselier plastic potential [6,7,8,22] is the sum of 3 terms, but the analytical form, deduced from thermodynamics and from the *generalized* normality rule, is different :

$$\frac{\sigma_{eq}}{1-f} - H(p,\dot{p}) + \sigma_1 D_1 f \exp\left(\frac{\sigma_m}{(1-f)\sigma_1}\right) = 0, \qquad 3\dot{\varepsilon}_m^p = \dot{p} D_1 f \exp\left(\frac{\sigma_m}{(1-f)\sigma_1}\right) \tag{5}$$

In the thermodynamics framework, the Kirchhof stress $\underline{\tau} = \underline{\sigma}/\rho$ has to be used in place of the Cauchy stress $\underline{\sigma}$, with $\rho \cong (1-f)/(1-f_0)$. Assuming $f_0 << 1$, only $\underline{\sigma}/(1-f)$ remains. The viscoplastic flow stress is $\sigma_{vp} = H(p,\dot{p})$. As in Rice and Tracey's original model and unlike the Gurson model, the under exponential denominator is a constant σ_1. Thermodynamics does not give the integration constants D_1 and σ_1. Generally, D_1=2 is adopted in applications. By analogy with Rice and Tracey's model, $Q\sigma_1 = (3/2)\sigma_1 = H(p_1,\dot{p})$ is assumed, with saturated strain hardening for a large parameter $p = p_1$ (Voce). If strain hardening does not saturate (Swift), σ_1 (or p_1) is a parameter to be calibrated [7,16]. σ_1 parametrically depends on strain rate $\dot{p}$ (and on temperature), which enabled to model the ductility curve in the range 10^{-3}-10^{+6} s^{-1}, including the "adiabatic nose" at very large strain rates (inertia effect) [17].

With Q = 3/2, the CCNLM Eq. (3_1) is achieved exactly at the vertex of the model on the σ_m axis (Fig. 1). Conversely, we can consider that the CCNLM, Eqs (3_1) and (3_2), has to be achieved over exactly the entire flow surface, in which case we obtain the same equation (1_1) and the same value $Q = 3/2$ by two totally different methods: micromechanics vs. thermodynamics, which further enhances the strength of the Rice and Tracey model. Because of this property, the first finite element calculations with crack initiation and propagation by void damage and strain localization in a plane could be carried out in 1981 [6].

At the vertex, the model does not verify the analytical solution of the hollow sphere under pressure, contrary to the Gurson model. This reflects a fundamental difference between the two models: *ductile void damage* (*without a defined geometric configuration of voids*) for the Rousselier model, *initial plasticity of a hollow sphere* for the original Gurson model. Between the two Cartesian axes, the slope of the flow surface varies in a much smaller interval than with the Gurson model: from $-D_1 f = -1/5$ to -3/2 for the parameters of Fig. 1, vs. 0 to $-\infty$. The transition between the two conditions Eqs (3_2) and (3_1) is thus very progressive and void damage remains significant even in pure shear (if there are voids!). The Rousselier model is operational in its original form [6] and with a very small number of parameters [7,16].

3 Ductile fracture multi-scale modeling

In self-consistent polycrystalline models, in each grain g = 1 à N with volume fraction $(1-f)f_g$, the stress $\underline{\sigma}_g$ is uniform. The flow stress in equation (5_1) is substituted with the one of the polycrystalline matrix [8]. Equation (5_2) is not modified.

$$\frac{\sigma_{eq}}{1-f} - \left(\sum_{g=1}^{N} f_g \underline{\sigma}_g\right)_{eq} + \sigma_1 D_1 f \exp\left(\frac{\sigma_m}{(1-f)\sigma_1}\right) = 0 \qquad (6)$$

The total plastic strain rate is [8] :

$$\underline{\dot{\varepsilon}}^p = (1-f)\sum_{g=1}^{N} f_g \sum_{s=1}^{M} \underline{m}_{sg}(\dot{\gamma}_s + \dot{\gamma}_s^C) + \frac{1}{3} D_1 f \exp\left(\frac{\sigma_m}{(1-f)\sigma_1}\right)\dot{\varepsilon}_{eq}^p \underline{1} \qquad (7)$$

where $\underline{m}_{sg}$ is the orientation matrix of each slip system s = 1 to M and $\underline{1}$ is the unit tensor. To simplify the presentation, the contribution of kinematic hardening to slip rates is not written; for $|\tau_s| - r_s \geq 0$:

$$\dot{\gamma}_s = \left(\frac{|\tau_s| - r_s}{K_v}\right)^n Sign(\tau_s - r_s),\ \tau_s = \underline{\sigma}_g : \underline{m}_{sg},\ r_s = R + \sum_{i=1}^{2} Q_i \sum_{t=1}^{M} H_i^{st}[1 - \exp(-b_i \gamma_t^{cum})] \qquad (8)$$

where $\gamma_s^{cum} = \int |\dot{\gamma}_s| dt$ is the cumulated slip. The parameters (R, Q_1, b_1, Q_2, b_2) and (K_v, n) define work hardening and viscosity, respectively. The two hardening matrices H_1 and H_2 define the self-hardening of the slip systems (diagonal terms equal to 1) and the "latent" hardening (non diagonal terms) of all systems by already activated systems, which enables to model non proportional loadings. The use of two (*constant*) matrices makes it possible to model the evolution of latent hardening with large deformation, depending on the material parameters b_1 and b_2 [5]. Moreover, texture evolution at very large deformation can be taken into account [18], but it is not as significant as in the applications to forming and the computation time is multiplied by a factor in the order of 2.

A second population of submicron voids is now considered in slip bands. A volume fraction f_s is introduced for each slip system. The rate is the sum of a growth term and a nucleation term:

$$\dot{f}_s = \left[(1-f_s)D_{12} f_s \exp\left(\frac{|\tau_s|}{\tau_{12}}\right) + A_2([\underline{\varepsilon}_g]_{eq}^p)\right]\left(\frac{1}{2}\right)(\dot{\gamma}_s + \dot{\gamma}_s^C) \qquad (9)$$

The growth term is a transposition of equation (5_2). A more specific micromechanical model remains to be established, taking into account in particular the void rotation. The most important term is the A_2 nucleation function. The Gaussian function of Chu and Needleman

[19] is retained, but with the plastic deformation of the grain instead of the macroscopic deformation, because the secondary voids mainly nucleates within the most deformed grains. This is an essential point for modeling. The flow function Eq. (6) becomes:

$$\frac{\sigma_{eq}}{1-f} - \left(\sum_{g=1}^{N} f_g \underline{\sigma}_g \right)_{eq} + \sigma_1 D_1 \left(f + \sum_{g=1}^{N} f_g \left[\sum_{s=1}^{M} f_s \right]_g \right) \exp\left(\frac{\sigma_m}{(1-f)\sigma_1} \right) = 0 \qquad (10)$$

The two equations giving $\underline{\sigma}_g$ ("β model" based on an auxiliary strain tensor $\underline{\beta}_g$ [18]), with and without secondary voids, differ in the same amount as equations (6) and (10), they are not written here to simplify the presentation (refer to [8], equation (25)).

In equations (7) and (9), the term $\dot{\gamma}_s^C$ has not yet been defined. It comes from the generalization for ductile fracture at the microscopic scale of the Coulomb brittle fracture model at the macroscopic scale [8,9]. For $\left|\tau_s\right| + c_0 \sigma_{ns} \geq R_0$, where τ_s and σ_{ns} are the shear and normal components of the grain stress $\underline{\sigma}_g$ on the system *s*, the slip rate $\dot{\gamma}_s^C$ is added to $\dot{\gamma}_s$. The novel feature of this model is to consider softening in the form $\left|\tau_s\right| + c_0 \sigma_{ns} = R_0 \exp(-b_0 \gamma_{cum}^C)$ where $\dot{\gamma}_{cum}^C = \int \left|\dot{\gamma}_s^C\right| dt$ is the cumulated Coulomb slip, with a small value for b_0 (typically $b_0 = 1$ or 2) so that softening is progressive with a significant dissipation of mechanical energy. This model makes it possible to localize the deformation in a plane. It corresponds to the trans-granular crystallographic fracture mentioned in the introduction. When b_0 goes to infinity, Coulomb's brittle fracture model without dissipation is recovered.

4 Application examples

4.1 Materials

Two materials are studied: an aluminum alloy extrusion for the automotive industry and a low-alloyed Mn-Ni-Mo steel for large forging parts of nuclear power plants. The numerous hardening parameters and the reduced texture of the highly anisotropic aluminum have been identified simultaneously on the basis of numerous mechanical tests [5]. A texture reduced to 2 orthotropic texture components ($N = 8$ orientations), Fig. 2a, gives good results. The two 12x12 hardening matrices (face-centered cubic crystallographic structure, $M = 12$) depend on 5 parameters each for non-diagonal terms, all included in the identification procedure.

The determination of a reduced isotropic texture (for steel) is more delicate. It takes several hundred random orientations to obtain a relatively isotropic behavior. In [4], a texture reduced to only $N = 14$ orientations has been identified on a mechanical test basis computed with isotropic behavior: single and biaxial tension in many directions of a plane, various tests with shear, tension-shear orthogonal path. For the calculations that follow, the uniformity of the orientation density on the 3D unitary hyper-sphere (in the 4D space) has been slightly improved with $N = 15$ orientations identified on the same basis, which seems to be close to the optimum possible with this method. An attempt with $N = 18$ was not successful. The "isotropic" texture of Fig. 2b is symmetric with respect to the RD and TD axes, which makes it possible to mesh only the 1/4 of a specimen which has the same symmetries, in particular the axisymmetric notched tensile specimen of Section 4.2.

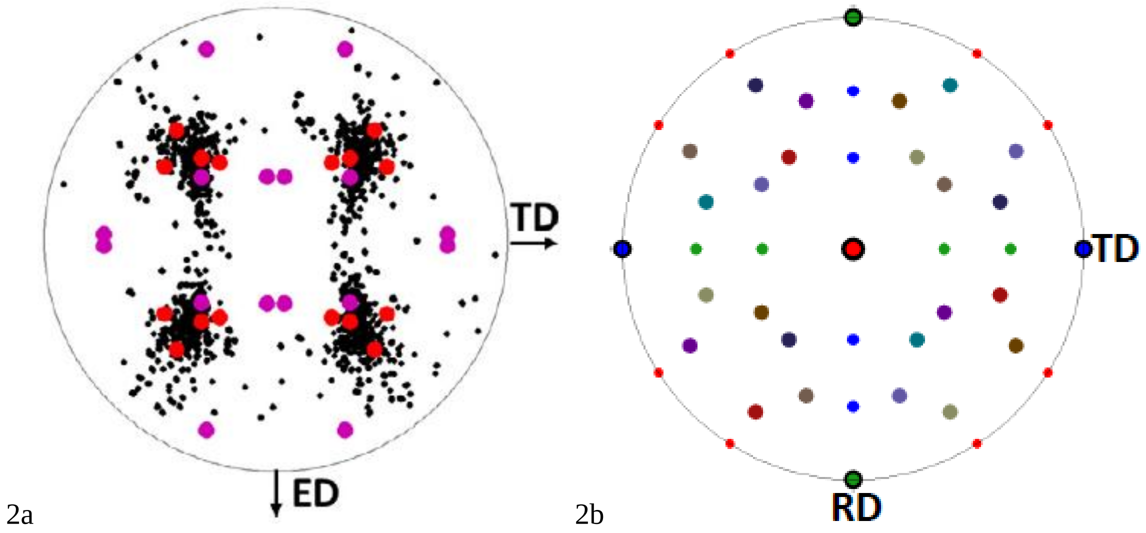

Figure 2. a) {111} pole figure of a 6260-T6 aluminum alloy extrusion (1 mm thickness central layer), black discs: EBSD measurements, colored discs: orthotropic texture reduced to 8 orientations.
b) {100} pole figure, equal area projection, "isotropic" reduced texture with 15 orientations.

With this isotropic "universal" texture (actually slightly anisotropic), it remains only to identify the hardening parameters on the tensile curve of the steel, from [20]. With the lack of at least one non-proportional experimental test, the coefficients of the hardening matrices could not be identified. For the centered cubic crystallographic structure of steel, $M = 24$ and the structure of the 24x24 hardening matrices is not well known. It is assumed that the non-diagonal terms of each matrix all have the same value (one parameter per matrix). The value $h = 0.1$ was chosen for the two matrices.

4.2 Finite elements calculations.

A "Butterfly" type shear specimen with a thickness of 1 mm in its central part was taken from the 2 mm thick aluminum extrusion [8]. The textures of Figure 2a correspond to the thickness of 1 mm. At large shear strain, the right and left edges of the specimen are in tension and two small cracks appear early and then stop, leading to a change of slope of the load-displacement curve. Shear cracking begins at quarter-width and causes a very rapid fall in applied load. After complete fracture of the specimen, no void could be observed in scanning electron microscopy (SEM) on the shear failure surfaces.

The experimental results and the numerical simulations are in good agreement for the localization of fracture, the strains at fracture and the fracture mechanisms at various scales. Fig. 3a shows the tensile lateral cracks and the shear cracks. The former are mainly due to the porous plasticity model (Fig. 3b) and the latter to the Coulomb-Rousselier model in ductile fracture at the slip system scale (Fig. 3c). More results are given in [8].

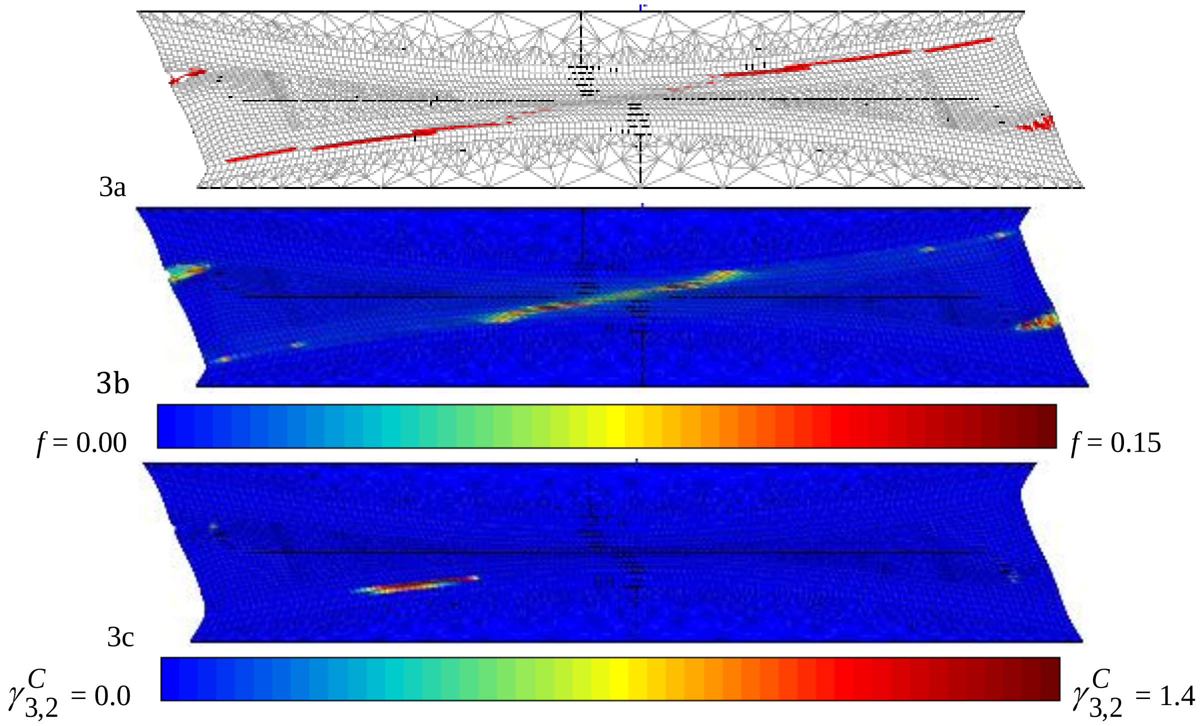

Figure 3. 6260-T6 aluminum alloy shear specimen : a) time=404, crack at mid-thickness ("broken" integration points in red), b) time=404, void volume fraction f, c) time=320, left: "Coulomb" cumulated slip ($g = 3$, $s = 2$), the slip system ($g = 2$, $s = 12$) forms a symmetric crack on the right (not shown in the figure) [8].

For steel, Fig. 4a shows the mesh (1/4) of the central part of the axisymmetric tensile specimen AE4 with a circular notch of radius 4 mm; the diameter of the minimum section is 10 mm. The load is applied in the vertical direction y = ND; the minimum section of the specimen is in the x-z = RD-TD plane of Fig. 2b. (Because of the slightly anisotropic reduced texture, the directions RD-TD-ND have to be specified.) The crack initiates in the center and propagates circularly over a *single layer* of integration points in the minimum section. The crack growth rate depends on the height of the elements, here 1/3 mm, in relation to the distance between the manganese sulfide (MnS) inclusions which initiate micrometric cavities from the beginning of plastic deformation in these steels : $f\,(\text{time}=0) = f_{\text{MnS}} = f_0$. Despite the symmetry, a 1/8 mesh is not to be used, it would generate a crack on two layers of integration points and therefore a double dissipation.

Submicron voids are observed with high magnification SEM on sections in the central zone corresponding to the two red elements of Fig. 4a [21]. They nucleate at large deformation (in part of the grains only) on carbides of average size 0.1 µm. The volume fraction of carbides is $f_{N2} = 0.024$ but at fracture in the center of the specimen the volume fraction of the carbides having initiated a void is only 0.006 (25%). This experimental data made it possible to recalibrate the two other parameters of the nucleation model: average initiation strain ε_{N2} = 0.7, standard deviation σ_{N2} = 0.15, see Fig. 4b: the nucleated fraction is larger in the part of the circular crack near the notch (red zones) because the strains are larger there at the beginning of the loading (notch effect). In the notch area, we can see on the left and right sections that the nucleation model at large strain can *contribute* to shear failure (red zones).

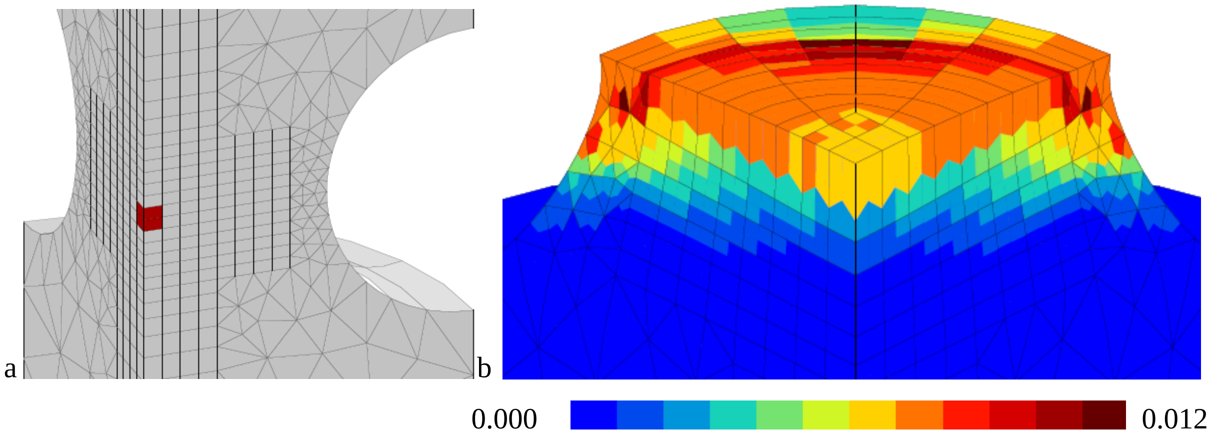

Figure 4. AE4 notched tensile specimen, f_0 = 0.0001 (small sulfur content) : a) Cartesian mesh in the specimen minimum section, b) volume fraction of carbides with nucleated submicron voids in the broken specimen, 0.006-0.007 in the center, light orange color, nucleated fraction $\cong$ 25% [21]. The layer of broken integration points is strongly stretched in the vertical direction, it corresponds to crack opening.

Calculations were made for two values of the initial void volume fraction: f_0 = 0.0001 and 0.0015, corresponding to small and large values of the sulfur content. In [21], f_{MnS} = 0.000175. The crack initiates in the elbow of the load-displacement curves (Fig. 5). The final shear fracture in the notch area causes a sudden load drop (red curve, f_0 = 0.0015).

When the sulfur content is large, the coalescence of the voids formed on the manganese sulfides occurs at smaller strains and only a small fraction of the carbides is nucleated and contributes to strain localization. Therefore, the submicron voids have little effect on the fracture resistance of the steel, the blue curve (with carbides) is close to the red curve (without carbides) for f_0 = 0.0015. The crack propagation rate (which determines the slope of the post-initiation curve) is a little larger with submicron voids than without. The effects of large contents of sulfur *and* carbon *do not cumulate*. Conversely, at small sulfur content, the fracture strains are larger and the voids nucleated on carbides greatly reduce the ductility.

In the notched tensile specimens, the loading paths at each point are not proportional because the plastic zone initiates in the notch and then propagates towards the axis. The damage in the center, crack initiation and propagation also induce non-proportional paths. The above calculations were performed with latent hardening parameter h = 0.1 for both hardening matrices.

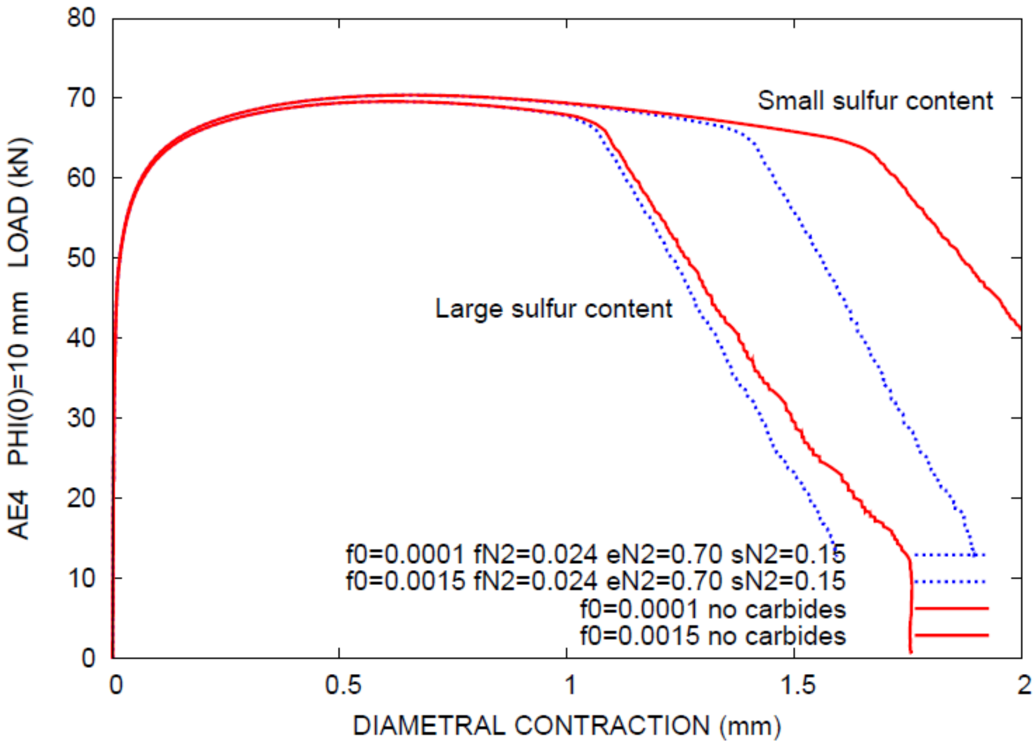

Figure 5. Load-displacement curves of the AE4 notched tensile specimen. Effect of sulfur and carbon contents in the MnNiMo low alloyed steel (voids nucleated on manganese sulfides and carbides, respectively).

Two other calculations were performed with h = 0.0 and 0.3. The hardening parameters have been identified in each case: an increase in h causes a sharp decrease in Q_1 and Q_2, R being little modified, Eq. (8). The *overall* effect in plasticity is rather small since the maximum force is 70.40-69.62-69.79 kN for h = 0.0-0.1-0.3; the difference of 1% between 0.0 and 0.1 is nevertheless significant. Conversely, the deformation at crack initiation is markedly increased for h = 0.0 (insert of Fig. 6). The absence of latent hardening is not realistic: a more complete study based on experimental tests and parameter calibration in plasticity and fracture would be necessary.

The deviation from isotropy is shown in Fig. 6 for y = ND = {001}, y = TD = {010} and y = {111} loading directions. The 1/4 mesh is used for the {010} and {111} directions, although the symmetry of the reduced texture in the xz plane is then imperfect. The direction y = RD = {100} gives results identical to TD (symmetry of the reduced texture). The load maximums are 69.62-69.04-68.30 kN, the dispersion is less than ± 1%. This significant but acceptable value is the price to be paid for the polycrystalline plasticity simulation of an isotropic material at a reasonable cost. For an anisotropic material with a reduced texture, it is likely that the difference in results with the real texture is of the same order of magnitude.

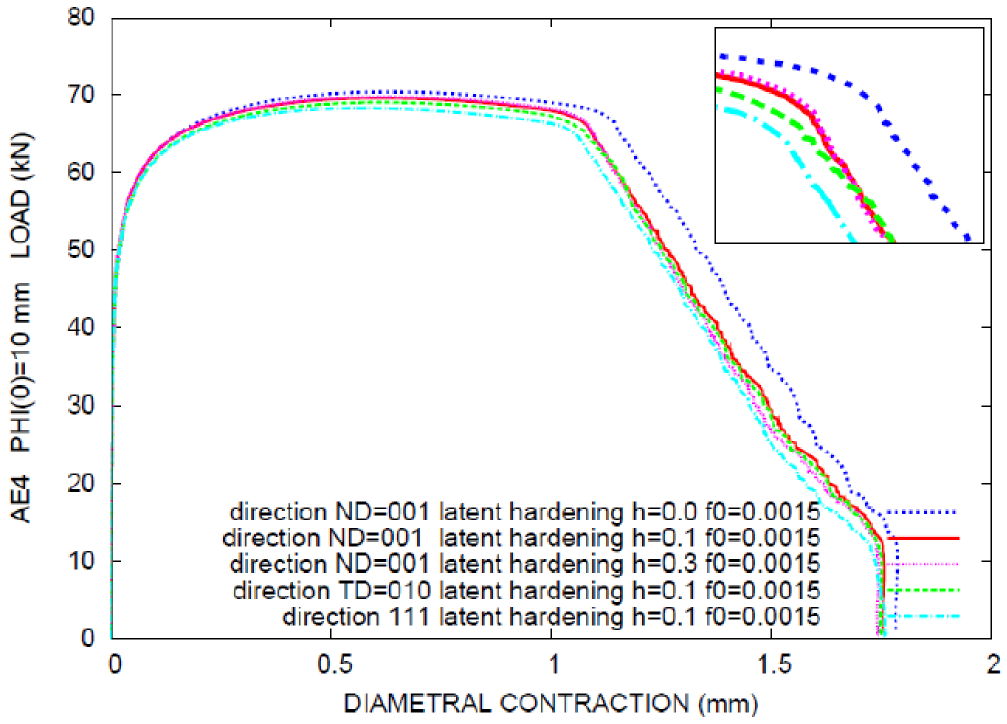

Figure 6. Load-displacement curves of the AE4 notched tensile specimen ($f_0 = 0.0015$). Latent hardening effect (ND tensile direction), tensile direction effect (for $h = 0.1$). All curves without secondary voids ($f_{N2} = 0$).

5 Conclusions

Rice and Tracey's founding model is a solid reference since it is in agreement with old or recent void growth measurements and it is obtained by two totally different methods: micromechanics vs. thermodynamics (via the Rousselier model), including the constant $Q = 3/2$ for the exponential effect of stress triaxiality. The Gurson model is the most widely used in its multiple versions (GTN, etc.) that aimed at making an initial yield surface model of the hollow sphere usable for ductile fracture. Conversely, the Rousselier model is operational in its original form with a very small number of parameters and it agrees (like Thomason's coalescence model) with the necessary kinematic condition of macroscopic localization (in a plane), which is not the case of the Gurson model.

Because of its analytical form, only the Rousselier model can be integrated into the multi-scale framework of self-consistent polycrystalline plasticity. This framework also makes it possible to model at the microscopic scale other mechanisms of plasticity, for example dynamic strain aging, and ductile fracture, for example trans-granular crystallographic fracture, observed in particular in thin aluminum sheets, or the effect of a second population of submicron voids in steels and aluminum alloys. Examples of numerical simulations of specimens are given for these two classes of materials. The polycrystalline framework provides results that are not accessible with macroscopic models and that can be compared with experimental data (mechanisms, quantitative observations at various scales).

References

[1] A. L. Gurson, Continuum theory of ductile rupture by void nucleation and growth: Part I-Yield criteria and flow rules for porous ductile media, J. Eng. Mater. Technol. 99 (1977) 2-15.

[2] V. Tvergaard, Influence of voids on shear band instabilities under plane strain conditions, Int. J. Fracture 17 (1981) 389-407.

[3] V. Tvergaard, A. Needleman, Analysis of cup-cone fracture in a round tensile bar, Acta Metall. 32 (1984) 157-169.

[4] G. Rousselier, F. Barlat, J.W. Yoon, A novel approach for anisotropic hardening modeling – Part II: anisotropic hardening in proportional and non-proportional loadings, application to initially isotropic material, Int. J. Plasticity 26 (2010) 1029-1049

[5] M. Luo, G. Rousselier, Modeling of large strain multi-axial deformation of anisotropic metal sheets with strength-differential effect using a Reduced Texture Methodology, Int. J. Plasticity 53 (2014) 66-89.

[6] G. Rousselier, Finite deformation constitutive relations including ductile fracture damage. In Nemat-Nasser, S., (Ed.), Three-dimensional constitutive relations and ductile fracture. North-Holland, Amsterdam, 1981, 319-343. 〈hal-02060680〉

[7] G. Rousselier, J.-C. Devaux, G. Mottet, G. Devesa, A methodology for ductile fracture analysis based on damage mechanics: an illustration of a local approach to fracture. In Landes, J., Saxena, A., Merkle, J., (Eds), Nonlinear Fracture Mechanics: Volume II, Elastic-Plastic Fracture, STP995V2-EB, ASTM International, 1989, 332-354. 〈hal-02081538〉

[8] G. Rousselier, M. Luo, A fully coupled void damage and Mohr-Coulomb based ductile fracture model in the framework of a Reduced Texture Methodology, Int. J. Plasticity 55 (2014) 1-24.

[9] G. Rousselier. Rupture ductile plate/inclinée, nouveaux matériaux : des défis pour la modélisation. 23ème congrès français de mécanique, Aug. 2017, Lille, France. 10 p., 2017. 〈hal-01634936〉

[10] G. Rousselier, T.F. Morgeneyer, S. Ren, M. Mazière, S. Forest, Interaction of the Portevin-Le Chatelier phenomenon with ductile fracture of a thin aluminum specimen: experiments and simulations, Int. J. Fracture 206 (2017) 95-122.

[11] A. Buljac, F. Hild, L. Helfen, T.F. Morgeneyer, On deformation and damage micromechanisms in strong work hardening 2198 T3 aluminum alloy, Acta Materialia 149 (2018) 29-45.

[12] J. R. Rice, D. M. Tracey, On the enlargement of voids in triaxial stress fields, J. Mech. Phys. Solids 17 (1969) 201-217.

[13] Y. Huang, Accurate dilatation rates for spherical voids in triaxial stress fields, J. Appl. Mech. 58 (1991) 1084-1085.

[14] J. Koplik, A. Needleman, Void growth and coalescence in porous plastic solids, Int. J. Solids Structures 24 (1988) 835-853.

[15] P. F. Thomason, Three-dimensional models for the plastic limit-loads at incipient failure of the intervoid matrix in ductile porous solids, Acta Metall. 33 (1985) 1079-1085.

[16] G. Rousselier, The Rousselier model for porous metal plasticity and ductile fracture. In Lemaitre, J., (Ed.), Handbook of Materials Behavior Models, Academic Press, San Diego, 2001, 436-445.

[17] G. Rousselier, Dissipation in porous metal plasticity and ductile fracture, J. Mech. Phys. Solids 49 (2001) 1727-1746.

[18] G. Rousselier, F. Barlat, J.W. Yoon, A novel approach for anisotropic hardening modeling – Part I: Theory and its application to finite element analysis of deep drawing, Int. J. Plasticity 25 (2009) 2383-2409.

[19] C.C. Chu, A. Needleman, Void nucleation effects in biaxially stretched sheets, J. Engrg. Mater. Technol. – Trans. ASME 102 (1980), 249-256.
[20] E. Lorentz, J. Besson, V. Cano, Numerical simulation of ductile fracture with the Rousselier constitutive law, Comput. Methods Appl. Mech. Engrg. 197 (2008) 1965-1982.
[21] B. Tanguy, Modélisation de l'essai Charpy par l'approche locale de la rupture, application au cas de l'acier 16MND5 dans le domaine de transition, thèse de l'Ecole Nationale Supérieure des Mines de Paris, 10 juillet 2001.
[22] P. Germain, Q.S. Nguyen, P. Suquet, Continuum thermodynamics. ASME. J. Appl. Mech., 50(4b) (1983), 1010-1020, https://doi.org/10.1115/1.3167184.